

Benchmarking Uncertainty Quantification of Plug-and-Play Diffusion Priors for Inverse Problems Solving

Xiaoyu Qiu¹ , Taewon Yang² , Zhanhao Liu² , Guanyang Wang³ , and
Liyue Shen²

¹Department of Statistics, University of Michigan,
`xiaoyuq@umich.edu`

²Department of EECS, University of Michigan,
`{taewony, zhanhaol, liyues}@umich.edu`

³Department of Statistics, Rutgers University,
`{guanyang.wang}@rutgers.edu`

February 5, 2026

Abstract

Plug-and-play diffusion priors (PnPDP) have become a powerful paradigm for solving inverse problems in scientific and engineering domains. Yet, current evaluations of reconstruction quality emphasize point-estimate accuracy metrics on a single sample, which do not reflect the stochastic nature of PnPDP solvers and intrinsic uncertainty of inverse problems, critical for scientific tasks. This creates a fundamental mismatch: in inverse problems, the desired output is typically a posterior distribution and most PnPDP solvers induce a distribution over reconstructions, but existing benchmarks only evaluate a single reconstruction, ignoring distributional characterization such as uncertainty. To address this gap, we conduct a systematic study to benchmark the uncertainty quantification (UQ) of existing diffusion inverse solvers. Specifically, we design a rigorous toy model simulation to evaluate the uncertainty behavior of various PnPDP solvers, and propose a UQ-driven categorization. Through extensive experiments on toy simulations and diverse real-world scientific inverse problems, we observe uncertainty behaviors

consistent with our taxonomy and theoretical justification, providing new insights for evaluating and understanding the uncertainty for PnPDPs.

1 Introduction

Inverse problems are ubiquitous and fundamental across diverse scientific and engineering applications, including astronomy [Craig and Brown, 1985], oceanography [Wunsch, 1996], medical imaging [Song et al., 2022b, Chung and Ye, 2022a], geophysics [Virieux and Operto, 2009], and audio signal processing [Lemercier et al., 2025, Moliner et al., 2023], among others. Recently, Plug-and-Play Diffusion Priors (PnPDP) have emerged as a promising paradigm for solving these inverse problems, leveraging the generative power of pretrained diffusion models to regularize solutions effectively [Chung et al., 2022, Chen et al., 2025, Cardoso et al., 2023, Song et al., 2024].

Despite rapid algorithmic advancements, evaluation and benchmarking efforts lag behind, typically focusing on a set of natural image restoration tasks such as image denoising and deblurring. [Kadkhodaie and Simoncelli, 2021, Song et al., 2023b, Mardani et al., 2023b]. Furthermore, to evaluate real-world scientific applications with greater structural challenges in forward modeling, where priors and observations are governed by underlying physics, Zheng et al. [2025] introduced InverseBench, a comprehensive evaluation of existing PnPDP methods focused on scientific tasks.

However, another gap on the evaluation objective remains. Natural image restoration tasks often reward pixel-wise accuracy (*e.g.*, Peak Signal-to-Noise Ratio (PSNR)) from a random reconstruction [Kadkhodaie and Simoncelli, 2021], whereas scientific applications require distributional correctness on the unobserved posterior, *i.e.*, calibrated uncertainty that preserves all physically valid solutions and enables principled risk quantification. This creates a potential misalignment: not only are we ignoring the inherent stochastic nature of diffusion generative solvers which can lead to multiple plausible reconstruction (Fig. 1), but we are also overlooking the critical role of uncertainty in scientific applications. This mismatch is evident in Fig. 2, where several PnPDP solvers produce similarly high-quality reconstructions under the same measurement, yet induce markedly different pixel-wise variance patterns across repeated runs.

We call this phenomenon the *Accuracy Trap*. As illustrated in Fig. 1, relying solely on point accuracy metrics (*e.g.*, PSNR) can fundamentally mischaracterize posterior samplers. For instance, an off-posterior reconstruction \hat{x}_2 may achieve a higher PSNR than a posterior-plausible reconstruction \hat{x}_3 simply because \hat{x}_2 happens to be closer to the ground-truth x^* . Moreover, different PnPDP solvers can exhibit qualitatively different uncertainty behaviors. Some solvers produce well-dispersed samples that largely

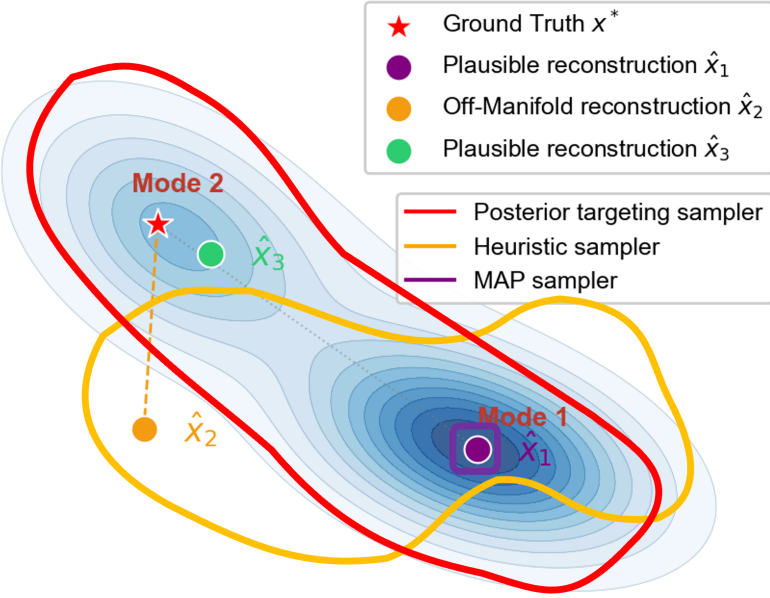


Figure 1: **Illustration of the *Accuracy Trap* phenomenon and three types of uncertainty behaviors.** Blue contours show the ground-truth posterior $p(x | y)$, which can be multi-modes. The red star denotes the ground-truth x^* ; \hat{x}_1, \hat{x}_3 are posterior-plausible reconstructions, while \hat{x}_2 is an off-posterior reconstruction that can be closer to x^* than \hat{x}_3 . The posterior targeting sampler (red) aims to match the posterior distribution and can represent uncertainty across modes. The heuristic sampler (orange) may generate samples both on and off the posterior support. The MAP-like sampler (purple) concentrates around a single mode.

reflect the posterior uncertainty, some generate a mixture of posterior-plausible and off-posterior samples, and others collapse to nearly deterministic outputs. Consequently, robust uncertainty quantification (UQ) is not an optional add-on, but a prerequisite for deploying PnPDP solvers in risk-sensitive scientific applications.

In the broader machine learning literature, UQ is often decomposed into aleatoric uncertainty(AU) and epistemic uncertainty(EU) [Hüllermeier and Waegeman, 2021], and recent work proposes single-model mechanisms to estimate these uncertainties [Hofman et al., 2024, Chan et al., 2024]. PnPDP solvers, however, operate in a different regime. Even with the same pretrained diffusion prior, multiple PnPDP solvers can induce markedly different reconstruction distributions given the same measurements. Accordingly, our goal is not to design another uncertainty estimator for a particular model, but to benchmark the uncertainty behavior of existing PnPDP solvers for inverse problems under a unified evaluation framework. Encouragingly, uncertainty has started to receive attention in diffusion-based inverse problems as well, for example as a signal for distribution shift [Kim and Fridovich-Keil, 2025]. Yet, to our knowledge, there is still no systematic framework

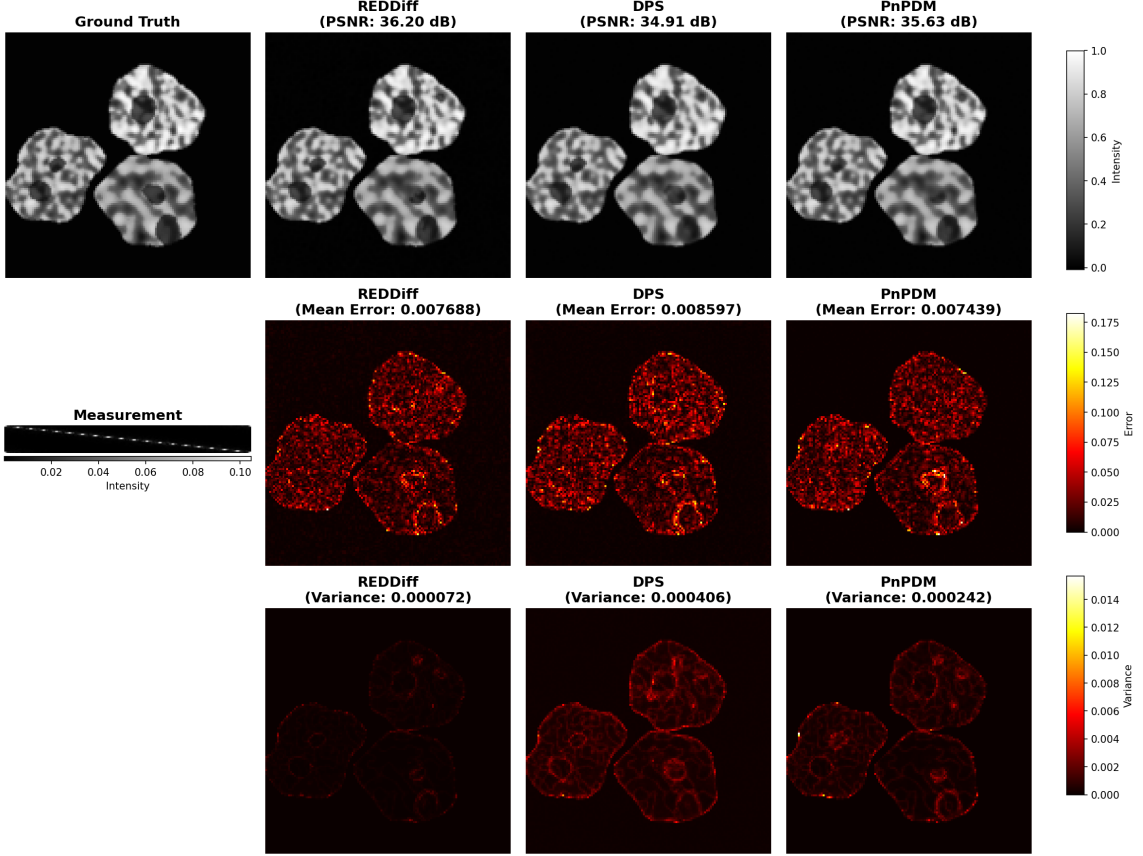


Figure 2: **Similar reconstruction with distinct uncertainty.** Comparison of PnPDP solvers on linear inverse scattering reconstruction with $K = 100$ times reconstruction on each solver. **Top two Row:** These methods produce similar reconstruction quality (in PSNR). **Bottom Row:** The pixel-wise variance maps reveal a fundamental difference. REDDiff[Mardani et al., 2023a] exhibits the lowest variance, while DPS[Chung et al., 2022] shows the highest uncertainty in structure-rich areas.

to assess whether the run-to-run variability produced by a PnPDP solver reflects valid posterior uncertainty, and how such variability differs across methods. This raises a central research question: *Can stochastic PnPDP solvers recover the posterior $p(x | y)$ and its uncertainty as defined by the inverse problem?*

Contributions. To address this gap, we propose a systematic study of uncertainty quantification (UQ) for PnPDP solvers in scientific inverse problems:

- We conduct a systematic study on UQ for diffusion model based inverse solvers, complementing the previous benchmark on PnPDP methods. We demonstrate that methods with comparable reconstructions can provide distinct uncertainty behavior.
- We design a rigorous toy model simulation with groundtruth available, to quantify the uncertainty of existing PnPDP methods compared to the ground truth posterior.

The results motivate a UQ-driven categorization of methods, supported by theoretical justification.

- We conduct various inverse problem tasks in real-world scientific applications and demonstrate consistent uncertainty behaviors across tasks, aligning with theoretical insights and our proposed UQ-driven categorization.

2 Preliminarily and Background

2.1 Inverse Problem

The inverse problem aims at reconstructing an unknown signal $x \in \mathbb{R}^n$ based on the measurements $y \in \mathbb{R}^m$. Formally, y derives from a forward process determined by Eq.1:

$$y = A(x) + \epsilon \quad (1)$$

where A can be either a linear operator, such as the Radon transform in sparse-view CT reconstruction and Fourier transform in accelerated MRI, or a nonlinear operator, such as the JPEG restoration encoder. A can also be either given or unknown. In this work, we focus on the situation where A is given. The term ϵ denotes random measurement noise.

2.2 Diffusion Models as Priors

Diffusion models [Song et al., 2021, Ho et al., 2020, Song et al., 2022a] have demonstrated extraordinary ability to generate high quality images. A diffusion model defines a forward noising process that transforms clean data $x_0 \sim p_{\text{data}}$ into noisy variables x_t for $t \in [0, T]$, and learns a network that enables reversing this process. In practice, the trained diffusion model can be viewed as providing either (i) *a score function* $s_\theta(x_t, t) \approx \nabla_{x_t} \log p_t(x_t)$ as in score-based DM[Song et al., 2021], or (ii) *a denoiser* that predicts a clean image $\hat{x}_0 = \text{Denoise}_\theta(x_t, t)$ from the initial noise x_t as in DDPM[Ho et al., 2020]. Throughout, we view the diffusion model as an *implicit distributional prior* that can be queried via the score function or denoising operations, when the prior density $\log p_\theta(x_0)$ is not available in closed form.

2.3 Diffusion Priors in Plug-and-Play Methods for Inverse Problem Solving

Plug-and-play diffusion prior (PnPDP) methods combine a pretrained diffusion model prior $p_\theta(x)$ with a known forward model to perform inference for the posterior:

$$p_\theta(x | y) \propto p(y | x) p_\theta(x), \quad (2)$$

where the prior term $p_\theta(x)$ comes from the diffusion model prior and the likelihood term $p(y | x)$ is determined by A and the noise model. The likelihood term enforces measurement consistency by favoring reconstructions that yield high $p(y | x)$. In practice, PnPDP algorithms impose measurement consistency via different mechanisms, including gradients[[Chung et al., 2022](#), [Zhang et al., 2024](#), [Wu et al., 2024](#)], projection[[Chung and Ye, 2022b](#), [Jalal et al., 2021](#), [Kawar et al., 2022b](#), [Wang et al., 2023](#), [Kawar et al., 2022a](#)], sampling[[Cardoso et al., 2023](#), [Dou and Song, 2024](#)], or other optimizations[[Mardani et al., 2023a](#), [Song et al., 2023a](#)].

Prior work has proposed different taxonomies for diffusion-based inverse solvers depending on the different criterion, such as algorithmic structure, optimization technique, or the type of inverse problem [[Daras et al., 2024](#), [Zheng et al., 2025](#)]. For example, InverseBench groups existing PnPDP methods mainly based on algorithmic structure, including linear guidance, general guidance, variable-splitting, variational Bayes, and sequential Monte Carlo [[Zheng et al., 2025](#)]. InverseBench further provides a comprehensive benchmark that evaluates reconstruction performance across diverse operators using standard accuracy metrics including PSNR and SSIM [[Zheng et al., 2025](#)]. While its structural taxonomy is useful for describing how methods couple a diffusion prior with the forward model, it is primarily descriptive, and methods within the same family can behave quite differently. This motivates us to seek a more user-facing categorization perspective that better reflects practical capability.

2.4 Limitation on Current Evaluation Metrics

Existing work mainly benchmarks the reconstruction quality by accuracy (*e.g.*, PSNR/SSIM). While accuracy metrics remain necessary, they are insufficient for evaluating PnPDP solvers. There are two fundamental reasons: (i) in ill-posed inverse problems the *target* is a posterior distribution $p(x | y)$ with many plausible reconstructions of the same measurement, and (ii) most PnPDP solvers are inherently *stochastic*, producing a distribution of reconstructions rather than a single deterministic output. Together, the object of interest is a distribution over reconstructions, motivating uncertainty-aware evaluation.

Reason 1: The target is a posterior distribution with ill-posed forward operator.

PSNR summarizes squared error to the ground-truth x^* and correlates with risk mainly when the inverse problem is well-posed and $p(x | y)$ is effectively unimodal. However, in ill-posed settings $y = Ax + \varepsilon$ ($x \in \mathbb{R}^n, y \in \mathbb{R}^m$), $m \ll n$ or $\text{rank}(A) \ll n$. Many distinct x can satisfy the measurement constraint.

Reason 2: PnPDP solvers are stochastic. Most PnPDP solvers are inherently stochastic, generating samples by injecting randomness through diffusion models so the output under a fixed measurement y is naturally a random variable $X | y$. Therefore, point metrics alone are insufficient to distinguish whether a solver is reliable or not. As demonstrated in Fig. 2, several solvers can yield similar reconstruction accuracy from a single sample, yet induce greatly different uncertainty. Existing evaluation benchmarks ignore this discrepancy, treating an overconfident solver and a calibrated solver as equivalent.

Table 1: **UQ-driven taxonomy of PnP diffusion methods and their relation to the InverseBench algorithm classes.** Our categorization groups methods by their ability to approximate the Bayesian posterior, complementing the mechanism-based classification in InverseBench.

Method	UQ-based Category (Ours)	InverseBench Category
MCG-Diff ([Cardoso et al., 2023])		Sequential Monte Carlo
FPS-SMC ([Dou and Song, 2024])	Posterior-targeting solvers	Sequential Monte Carlo
PnP-DM ([Wu et al., 2024])		Variable-splitting
DPS ([Chung et al., 2022])		General guidance
DAPS ([Zhang et al., 2024])		Variable-splitting
DDRM ([Kawar et al., 2022a])	Heuristic solvers	Linear guidance
DDNM ([Wang et al., 2023])		Linear guidance
DiffPIR ([Zhu et al., 2023])		Variable-splitting
ReD-diff ([Mardani et al., 2023a])	MAP-like solvers	Variational Bayes

3 Uncertainty-driven Benchmark for PnPDP Solvers

3.1 Epistemic and Aleatoric Uncertainty in Inverse Problems

Uncertainty in machine learning is commonly categorized into *epistemic uncertainty* (EU) arising from lack of knowledge, and *aleatoric uncertainty* (AU), arising from inherent stochasticity [Kendall and Gal, 2017]. In inverse problems, EU comes from limited measurements by illposed forward operator, and model misspecification induced by mismatching or imperfect learned priors, while AU comes from intrinsic randomness in the data generation process, such as the random measurement noise [Nagel and Sudret, 2016].

Conceptually, EU can be reduced by increasing the information from the measurements or improving the diffusion prior, and AU is irreducible.

In this benchmark, we assume the prior diffusion model is well-trained and fixed, therefore we focus uncertainty generated by the inverse problem $y = Ax + \varepsilon$, where AU is governed by the measurement noise $\varepsilon \sim N(0, \sigma^2 I)$ and EU is governed by the loss of information from the rank-deficient forward operator A (*e.g.*, undersampling). Here "more data" can reduce EU by collecting more informative measurements for the same underlying image (*e.g.*, increasing the sampling density).

3.2 Uncertainty Metrics and Interpretation

Beyond the commonly used accuracy metrics (*e.g.*, MSE, PSNR, SSIM), we quantify pixelwise uncertainty using the empirical posterior variance $\widehat{\text{Var}}(j) = \frac{1}{K-1} \sum_{k=1}^K (x^{(k)}(j) - \bar{x}(j))^2$ by running each method K times for each test case with independent initial noise to obtain samples $\{x^{(k)}\}_{k=1}^K$ from the solver generated reconstruction distribution. The empirical variance computed from repeated reconstructions is intended to approximate the variance of solver induced posterior distribution. The posterior variance in the inverse problems reflects the combination of AU from measurement noise and EU from illposedness, and is therefore neither "the larger the better" nor "the smaller the better."

Since AU and EU cannot be separated from the samples and the groundtruth posterior variance is generally unavailable in real-world inverse problems, we use controlled toy simulations in Sec. 4 to validate each PnPDP method from two aspects: (i) AU calibration under a fully observed measurement $A = I$ and (ii) uncertainty structure under a decoupled forward operator.

On the real data tasks where groundtruth posterior variance is unavailable, we focuses on relative comparisons across methods and tasks. For each task, we compute an accuracy score together with an uncertainty score from pixel-wise variance derived from multi-run independent samples, and analyze how their uncertainty behaviors perform across different test images, measurement sparsity and tasks.

3.3 A UQ–driven Category of PnPDP Methods

We reinterpret PnPDP inverse solvers through the perspective of their ability to capture posterior uncertainty. Rather than grouping methods by algorithmic structure, we ask a more fundamental question: **Can the sampling procedure reliably approximate the posterior $p(x | y)$?**

This capability-driven view induces three families: (i) *Posterior targeting solvers*: These algorithms are designed to target the true Bayesian posterior $p(x | y)$ and are

asymptotically consistent under standard assumptions; (ii) *Heuristic solvers*: Their variability is partially algorithm induced and not guaranteed to match posterior uncertainty; and (iii) *MAP-like solvers*: Their outputs collapse to one or a small set of modes, usually from optimization.

(i) Posterior-targeting solvers. Methods such as MCG-Diff [Cardoso et al., 2023], FPS-SMC [Dou and Song, 2024] and PnPDM [Wu et al., 2024] are *posterior-targeting*, in the sense that they are designed for an explicit Bayesian target. Under standard idealizations, their sampling distribution provably approaches the Bayesian posterior $p(x \mid y)$; see Appendix B for a unified summary of theoretical guarantees. This distinguishes them from other stochastic solvers whose randomness is partly or primarily algorithm-induced rather than linked to a target posterior measure. These methods provide *inherent* UQ capability: increasing computation (e.g. more particles or longer chains) typically improves posterior fidelity. However, there is often a large gap between the asymptotic theory and engineering practice: with high dimensional data, finite compute, and approximate operator evaluations, posterior-targeting solvers can exhibit bias, degeneracy, or collapse.

(ii) Heuristic solvers. These methods produce stochastic reconstructions and can yield informative variability maps, but they are not posterior-targeting in general. Unlike *posterior-targeting solvers* with a provable convergence to the posterior distribution, these heuristic methods enforce measurement consistency through algorithmic heuristics combined with a diffusion prior. Their variability typically comes from heuristic design choices such as surrogate guidance terms or splitting data-consistency steps with noise injection along the diffusion trajectory. As a result, the variability of these approaches can reflect a mixture of measurement uncertainty and algorithm-induced uncertainty effects. They often produce visually plausible reconstructions and some solvers can exhibit reasonable uncertainty patterns, but without guarantees of the posterior.

(iii) MAP-like solvers. These methods are formulated and used as point estimators, typically by optimizing a posterior objective $\min_x \frac{1}{2\sigma_y^2} \|Ax - y\|^2 + \lambda\phi(x)$, (e.g., $\phi(x) = \|\nabla x\|_1$ in TV [Rudin et al., 1992] and using the implicit diffusion score in Mardani et al. [2023a]), causing the output to collapse around a small set of modes and do not provide distributional uncertainty information.

Remark on heuristic solvers and MAP-like solvers. Several *heuristic solvers* [Zhu et al., 2023, Wang et al., 2023, Kawar et al., 2022a] also perform MAP in data-consistency substeps on the observed components via projection or pseudo-inverse updates. However,

these methods remain stochastic guided diffusion procedures overall (*e.g.*, through diffusion trajectory noise), thus categorized as *heuristic solvers*.

4 Diagnostic Toy Simulation

We first validate sampling fidelity using a linear inverse problem ($y = Ax + \epsilon$) with a Gaussian Mixture Model (GMM) prior $p(x)$. This setup provides a known, highly multimodal posterior, enabling precise assessment of a nontrivial prior and posterior with ground truth. We train the diffusion prior using a large amount of simulated data to ensure a high quality prior and to reduce the EU from misspecified prior as much as possible. Therefore, the remaining EU in the toy simulation is primarily by the illposedness in the inverse problem. Detailed experiment setups and steps are provided in Appendix D.1.

4.1 Experiment 1: AU (measurement noise) Recovery Under Identity Forward Operator $A = I$

Under $A = I$, the inverse problem is fully observed and introduces no uncertainty from forward operator, thus posterior uncertainty arises solely from the measurement noise, *i.e.*, purely AU. If a solver samples from the posterior, its empirical variance $\hat{\sigma}^2$ in this setting should reflect this measurement uncertainty. Practically, we generate $N = 100$ samples for a fixed y and repeat this over $K = 20$ test measurements $\{y_k\}$, then construct the 95% confidence interval using the empirical mean and variance. Under the fully observed $A = I$ with gaussian measurement noise, the 95% interval $\mu \pm 1.96\sigma$ should achieve approximately 95% empirical coverage when the method accurately samples from the true posterior. This is a necessary but not sufficient condition: while passing this test does not guarantee success in complex ill-posed settings, failing it indicates a fundamental inability to recover even the basic AU.

4.2 Experiment 2: Decoupling AU vs. EU via the Observed and Null-Space

Distinguishing between uncertainty in the observed and null spaces is also a prerequisite for reliable uncertainty quantification (UQ). However, in generic inverse problems (*e.g.*, MRI/CT), measurement noise and ill-posedness are deeply coupled, making it difficult to diagnose. To obtain a clean diagnostic, we design a controlled forward operator A with binary singular values $S_j \in \{0, 1\}$, which perfectly separates the observable subspace (\mathcal{J}_{obs}) and the null subspace ($\mathcal{J}_{\text{null}}$). In this setting, uncertainty in \mathcal{J}_{obs} should be dominated by

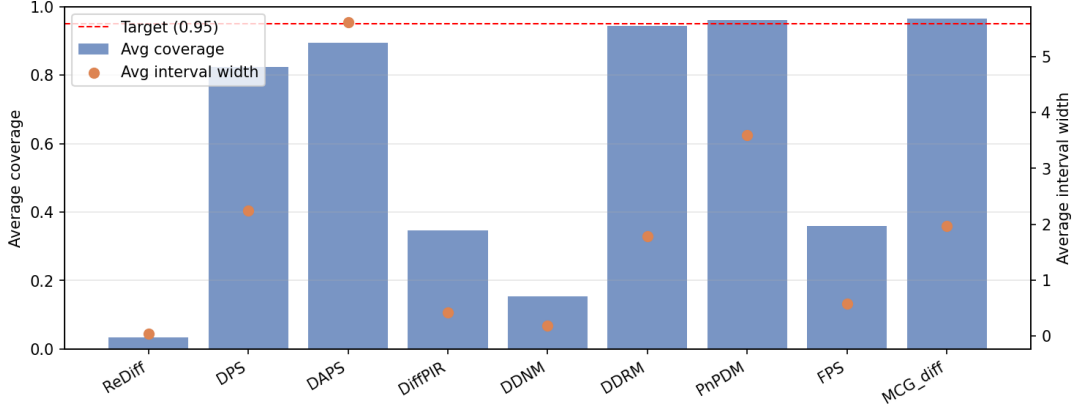


Figure 3: Average 95% coverage across methods (bars), with mean interval width marked as dots. The dashed line indicates the nominal 0.95 target; bars around 0.95 indicate better calibration, while higher dots indicate wider intervals.

AU as these directions is fully informed from the measurement, while uncertainty in $\mathcal{J}_{\text{null}}$ is combined of both AU and EU, since there is no information from measurements along these directions. Ideally, a calibrated solver should recover the uncertainty in both the \mathcal{J}_{obs} and $\mathcal{J}_{\text{null}}$.

4.3 Findings

Experiment 1 (Fig. 3): calibration under a fully observed operator ($A = I$). Figure 3 reports the empirical coverage at the 95% level and the corresponding interval width under $A = I$. **REDDiff** yields near-zero empirical variance and correspondingly near-zero coverage, consistent with the behavior of MAP solvers. Among stochastic solvers, **DDRM**, **PnPDM** and **MCG-Diff** achieve coverage close to the 95% target with moderate interval widths, indicating reasonably calibrated variability in this fully observed regime. In contrast, **FPS** severely underestimates potentially due to the SMC degeneracy under a multimodal posterior. Several heuristic solvers also show substantial under-coverage (*e.g.*, **DiffPIR**, **DDNM**, **DPS**), while **DAPS** attains closer-to-target coverage by producing much wider intervals.

Experiment 2 (Fig. 4): uncertainty structure across observed vs. null directions. Figure 4 demonstrates the mean variance in the observed subspace (Var_{obs}) and the null subspace (Var_{null}), along with the corresponding ground-truth references. **PnPDM** and **MCG-Diff** recover nontrivial variance in both subspaces, and matching the expected pattern that uncertainty should be higher along null directions than along well-observed ones, though **PnPDM** overestimate both while **MCG-Diff** slightly underestimate the null variance. **FPS** behaves qualitatively differently: its empirical null direction variance is largely out of

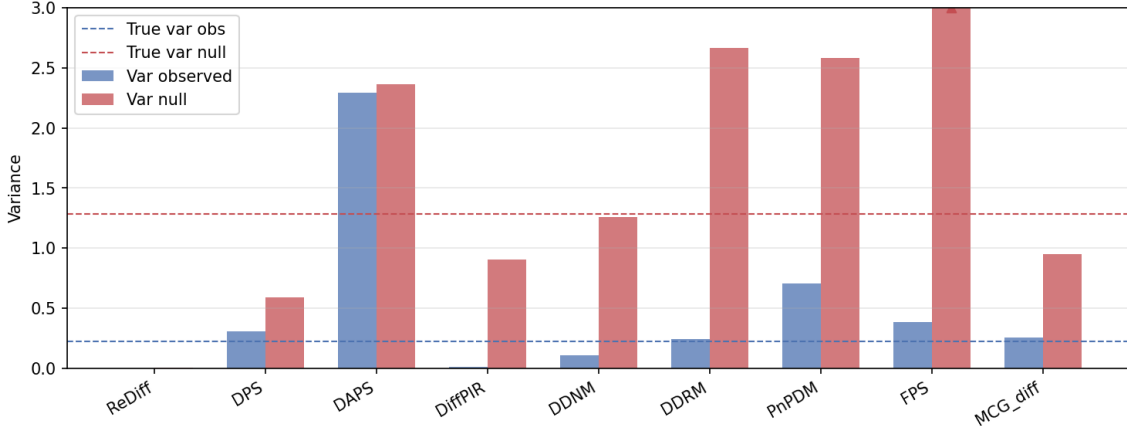


Figure 4: Observed- and null-space posterior variances in paired bars, with null/observed ratio shown as dots. Dashed lines mark the theoretical variances and solid line marks the theoretical null/observed ratio; points or bars beyond the axis limit indicate overflow.

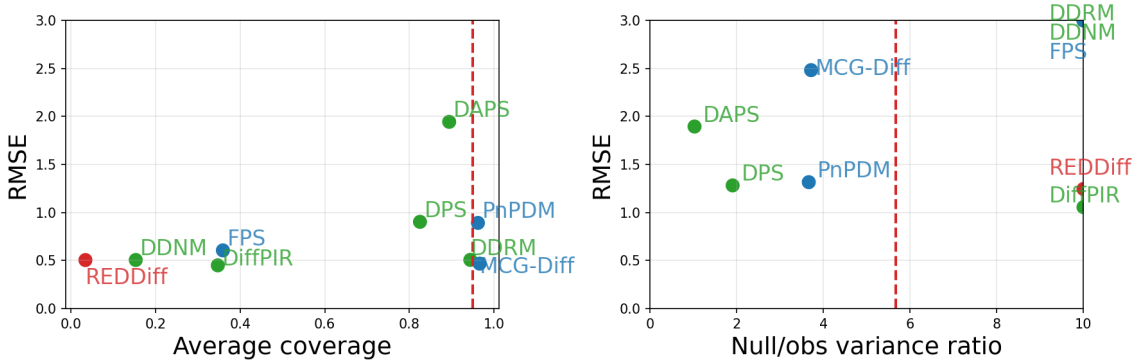


Figure 5: Accuracy–UQ scatterplots. Left: RMSE versus average coverage in Exp.1 ($A=I$). Right: RMSE versus null/observed variance ratio in Exp.2 (0–1 singular value). Points are color-grouped by method family; lower RMSE indicates better reconstruction accuracy, while coverage/ratio summarizes uncertainty calibration.

the figure limit, reflecting numerical instability triggered by zero singular values due to its reliance on inverse of A . This highlights a gap between asymptotic guarantees with practical settings and implementations. Heuristic solvers show heterogeneous patterns: DAPS markedly inflates Var_{obs} , while methods such as DiffPIR/DDNM almost recover the null variance but underestimate observed variance in Experiment 2. DPS can generate visually high-contrast variance maps, but its Var_{null} behavior is not consistently aligned with the operator-implied ambiguity.

Accuracy vs. uncertainty quantification. Figure 5 relates reconstruction accuracy (RMSE) to the previous two UQ diagnostics: empirical coverage (left) and the null/observed variance ratio (right). From the left figure, multiple solvers achieve similarly low RMSE (around 0.5) but exhibit drastically different coverage, with coverage spanning from severe under-coverage (≈ 0.1) to near-nominal (≈ 0.95). For the right figure, MCG-Diff is among

the methods that better preserve the observed and null space variance as observed from Fig. 4, yet its RMSE is not the smallest. In contrast, some solvers attain low RMSE while not producing reasonable variance, indicating misplaced or collapsed uncertainty. Overall, these results again reinforce that point accuracy metrics are insufficient for evaluating stochastic inverse solvers, and must be complemented with uncertainty quantification.

5 Real Data Experiments

5.1 Experiment Setup

Tasks and Datasets. We evaluate the uncertainty quantification performance of PnPDP solvers on three representative real-data inverse problems: (i) *linear inverse scattering*, (ii) *sparse-sampling MRI reconstruction*, and (iii) *sparse-view CT reconstruction*.

For the linear inverse scattering (data from [Wiesner et al., 2019]) and multi-coil MRI (fastMRI knee data from [Zbontar et al., 2019]), we follow the corresponding experimental setups in InverseBench [Zheng et al., 2025], respectively. For inverse scattering we consider the number of receivers $M = 180, 360$, while for sparse-sampling MRI, we evaluate $\times 4$ and $\times 8$ acceleration rate (AR).

For sparse-view CT (SVCT) task, we conduct experiments using the LIDC-IDRI dataset [Armato et al., 2011]. The original CT volumes are resampled to a slice thickness of 1 mm, and each slice is resized to 256×256 . The training set consists of 23,040 images, and in-distribution evaluation is conducted on the hold-out data. The diffusion model is trained using the pipeline proposed in [Karras et al., 2022] and the same trained model is used for all PnPDP methods.

For out-of-distribution (OOD) evaluation, we use Lung-PET-CT-Dx dataset [Li et al., 2020] from cancer patients. The bounding boxes for tumor region are provided with annotations from clinicians. We directly use the pretrained diffusion models from LIDC-IDRI dataset as the prior for reconstructing images from Lung-PET-CT-Dx dataset without any adaptation, thus as OOD task with imperfect or mismatch priors. Due to task feasibility, MRI and CT experiments include only REDDiff, DPS, DAPS, DiffPIR, and PnPDM, while inverse scattering includes all methods.

Sampling protocol. Given a trained diffusion prior \mathcal{D} for each task, each solver produces K posterior samples by rerunning its sampling procedure $\{x_n^{(k)}\}_{k=1}^K \sim \text{Method}(y_n; \mathcal{D})$, $K = 100$, with independent random seeds fixed across solvers: For each test instance $n \in \{1, \dots, N\}$ with ground-truth image x_n^* , we generate measurements as $y_n = A_t x_n^* + \varepsilon$, $\varepsilon \sim \mathcal{N}(0, \sigma^2 I)$, where A_t is the task-specific forward operator and σ is the noise level. We

Table 2: Results on 20 view CT tasks with in and out-of-distribution test image, and MRI with AR = 4. Pixel Var is scaled by $\times 10^3$.

Method	CT (in-distribution)			CT (out-of-distribution)			MRI Knee (AR = 4)		
	PSNR	SSIM	Pixel Var	PSNR	SSIM	Pixel Var	PSNR	SSIM	Pixel Var
REDDiff	30.755 \pm 0.094	0.848 \pm 0.002	0.298	25.306 \pm 0.094	0.739 \pm 0.003	0.521	31.298 \pm 0.037	0.743 \pm 0.001	1.250
DPS	31.333 \pm 0.167	0.813 \pm 0.023	0.305	24.575 \pm 0.190	0.671 \pm 0.017	0.578	28.069 \pm 0.140	0.622 \pm 0.004	3.582
DAPS	28.034 \pm 0.082	0.770 \pm 0.003	0.171	24.865 \pm 0.069	0.701 \pm 0.003	0.185	25.809 \pm 0.023	0.427 \pm 0.001	4.651
DifFPIR	22.803 \pm 0.214	0.659 \pm 0.011	0.844	19.712 \pm 0.100	0.506 \pm 0.010	0.901	30.209 \pm 0.045	0.690 \pm 0.002	1.599
PnPDM	27.619 \pm 0.568	0.803 \pm 0.010	0.329	24.049 \pm 0.229	0.701 \pm 0.006	0.464	31.781 \pm 0.037	0.766 \pm 0.001	0.977

use $K = 100$ since the empirical per-pixel sample variance stabilizes around this range (Appendix C). Unless otherwise stated, we adopt the solver hyperparameters from Table 12 of InverseBench [Zheng et al., 2025] for tasks (i) and (ii); for the CT task, hyperparameters are tuned separately following standard validation procedures.

Evaluation metrics. We report PSNR and Structural Similarity Index Measure (SSIM) as generic reconstruction accuracy metrics. For each solver and test instance, we compute PSNR and SSIM over $K = 100$ stochastic reconstructions and summarize their maximum, mean values. To assess uncertainty, we compute the pixel-wise sample variance across reconstructions, defined as $\text{Var}(x)_i = \frac{1}{K-1} \sum_{k=1}^K (x_i^{(k)} - \bar{x}_i)^2$, where \bar{x}_i denotes the sample mean at pixel i . We report both the full pixel-wise variance map and the variance averaged over pixels in the tables. We additionally quantify metric-level uncertainty via the sample variance of PSNR and SSIM across the K reconstructions.

We summarize real-data results using three complementary views: (i) quantitative results with both accuracy and variance metrics across three tasks (Table 2); (ii) qualitative results with reconstructions, error maps and variance maps (e.g., Figs. 7 and 9), and (iii) an accuracy–uncertainty summary plot (Fig. 6). In the qualitative figures, the top row shows the highest-PSNR reconstruction among the $K = 100$ samples for each solver (PSNR reported); the middle row shows the corresponding error map with mean absolute error over pixels; and the bottom row reports the pixel-wise variance map aggregated over all K samples, together with the spatially averaged variance reported.

To assess generalization, we also evaluate solvers across multiple test images under the same measurement, as well as across different measurement regimes (e.g., , receivers or acceleration rates) and tasks. Additional quantitative and qualitative results are provided in Appendix A.2.

5.2 Results and Findings

How do different solvers compare with each other in terms of uncertainty? Several solvers that achieve similar PSNR and visual reconstruction quality, can exhibit substantially different uncertainty behaviors, both in the magnitude and the spatial

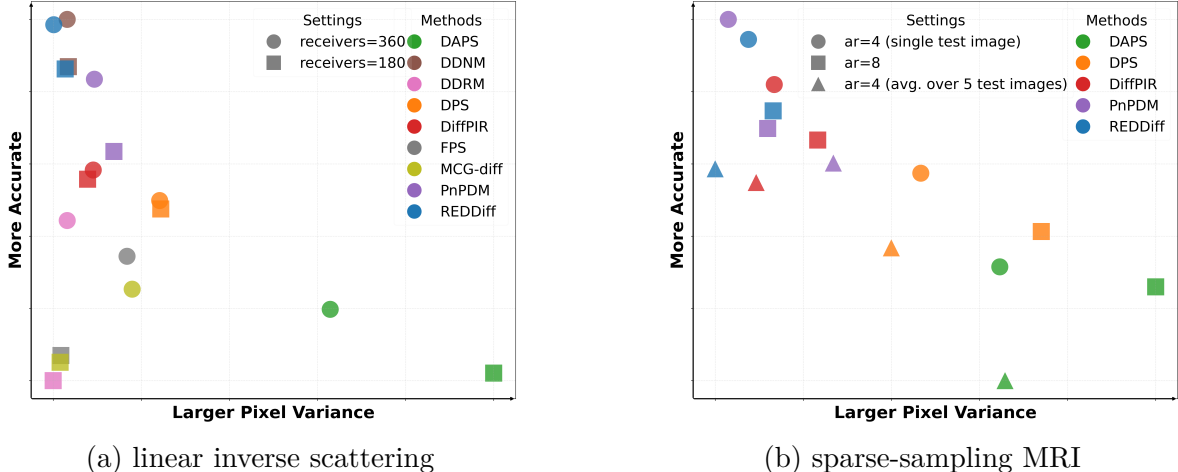


Figure 6: Normalized reconstruction accuracy (PSNR) versus pixel-wise uncertainty. Each point represents a solver under a specific measurement regime. For each subplot, PSNR and pixel-wise variance are independently min–max normalized across all evaluated solvers, mapping the largest and smallest values to 1 and 0, respectively.

structure of the estimated variance. For example, DAPS consistently produces a visible background variance across settings in Fig. 7 and 9, and also yields inflated variance along observed directions in Toy Experiment 2 (Fig. 4). Solvers also differ in the stability of their uncertainty behavior across tasks: the MAP solver REDDiff repeatedly shows near-zero variance, consistent with its point-estimation nature, whereas some heuristic solvers are less stable across settings. In particular, DPS shows relatively small variance in Toy Experiment 2 and the CT task, but much larger variance in linear inverse scattering and MRI. This variability is likely driven by sensitivity to algorithmic hyperparameters.

How does uncertainty vary with measurement sparsity? As measurement sparsity increases (*e.g.*, fewer receivers in inverse scattering or higher acceleration rates in MRI), most solvers exhibit increased pixel-wise variance (Tables 3 and 4). This trend is also visible in Fig. 6, for linear inverse scattering, points with 180 receivers (square) are generally shifted towards higher variance compared to corresponding 360-receiver setting (circle), and similarly for MRI. An exception is observed for the posterior-targeting solvers FPS and MCG-Diff, which suffer from particle collapse with the sparse 180-receiver setting, leading to degraded variance estimates. Overall, these results align with the intuition that inverse problems become more uncertain as observations become less informative.

How does uncertainty behavior relate to accuracy performance? In principle, reconstruction accuracy and uncertainty quantification are not necessarily related. For instance, REDDiff often achieves strong accuracy but produces near-zero variance, which is not a meaningful representation of uncertainty. Moreover, higher accuracy does not

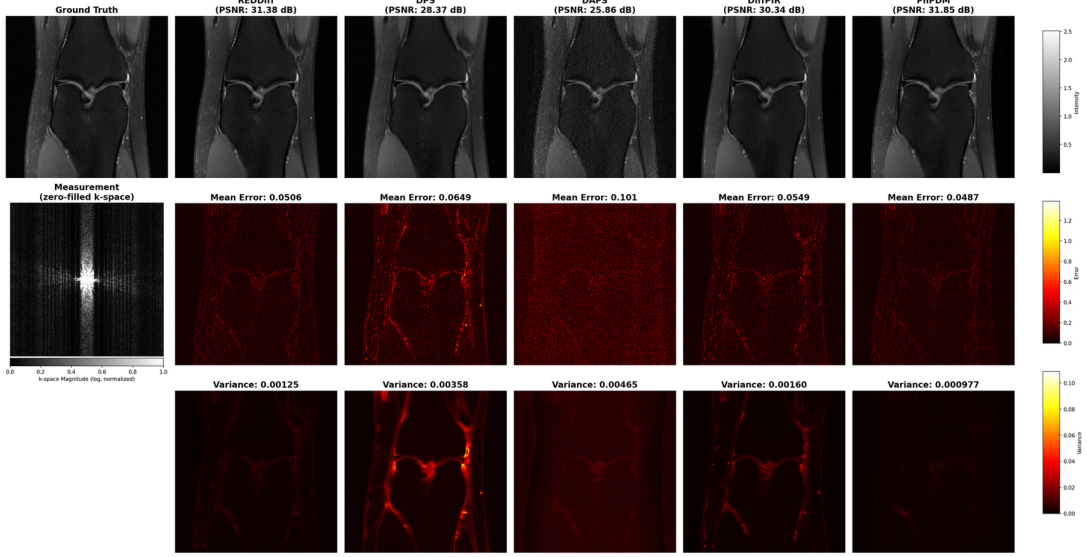


Figure 7: Sparse-sampling MRI under $\times 4$ acceleration rate (AR=4).

imply larger or smaller variance: in the 360-receiver inverse scattering (Fig. 9), DDNM and DDRM differ by roughly 5 dB in PSNR yet exhibit very similar variance levels. These results highlight that accuracy and uncertainty capture two independent aspects of PnPDM solvers, and both must be evaluated explicitly. These phenomenon are consistent with our toy simulation results (Fig. 5), where solvers with similar RMSE have largely different coverage, and some solvers achieve lower RMSE do not recover the observed and null direction variance well.

How do posterior targeting solvers relate their uncertainty behavior to theory? For FPS and MCG-Diff, increasing particle size N leads to more reasonable variance estimation, see Appendix A.3 for more details.

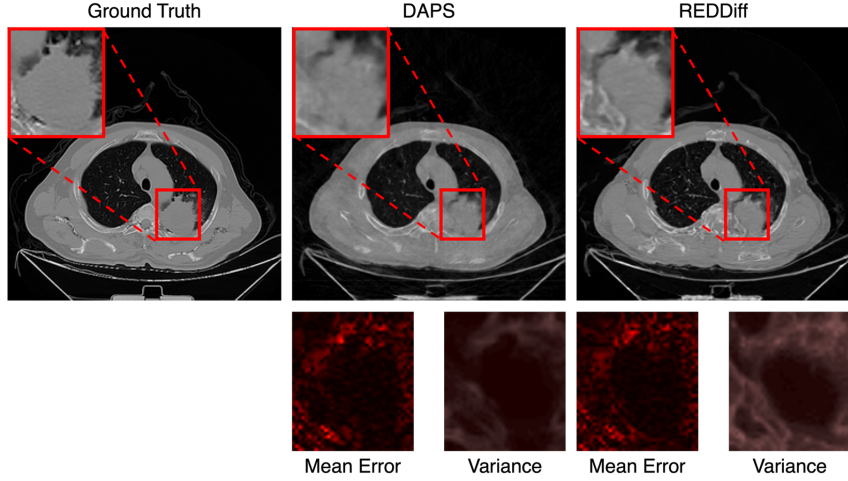


Figure 8: Out-of-distribution reconstruction result of 20-view CT using DAPS and REDDiff. The red bounding box shows the cancer region annotated by clinicians. The average PSNR of the entire image is 24.894 dB and 25.306 dB respectively while the average PSNR of the cancer region is 23.728 dB and 23.218 dB.

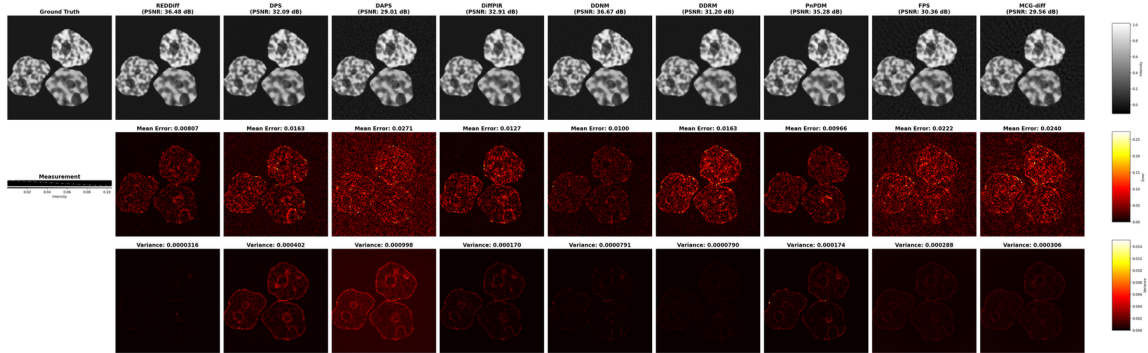


Figure 9: Inverse linear scattering with 360 receivers

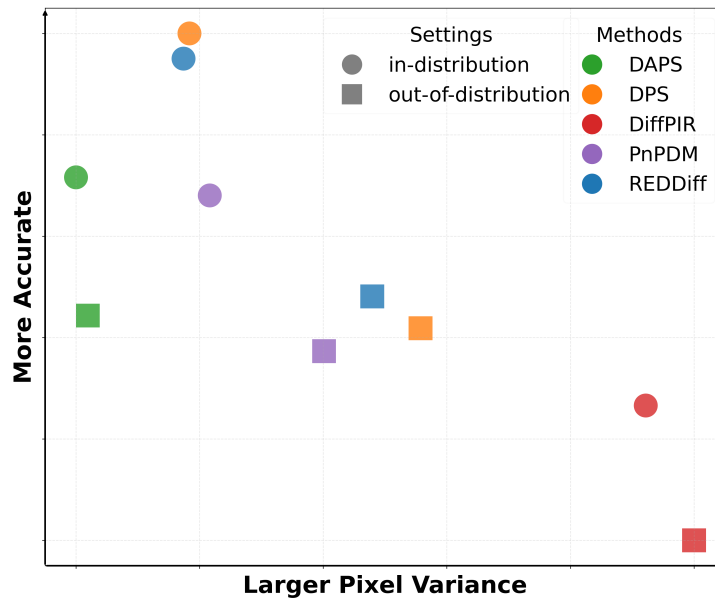


Figure 10: Sparse view CT: Normalized reconstruction accuracy (PSNR) versus pixel-wise uncertainty.

How does uncertainty behave in OOD reconstruction? Different solvers shows different behaviors on OOD compared with in-distribution reconstruction. As illustrated in Fig. 8, DAPS produces visually reasonable reconstruction but does not exhibit an increase in uncertainty at the tumor region for OOD test image, while other solvers exhibit an obvious increase in uncertainty on the OOD image(Fig. 10).

6 Discussion and Conclusion

In this paper, we benchmark uncertainty quantification for PnPDP solvers in inverse problems. We show that solvers with similar reconstruction quality can exhibit greatly different uncertainty behavior, and use toy simulations together with multiple real-data studies to reveal consistent uncertainty behaviors across different regimes. One limitation is the limited evaluation of hyperparameter sensitivity across methods, left for future work. We hope this work can inspire uncertainty-aware diffusion sampler design in future works.

Acknowledgment

Guanyang Wang acknowledges support from the National Science Foundation through grant DMS-2210849 and an Adobe Data Science Research Award. Liyue Shen acknowledges funding support by NSF (National Science Foundation) via grants IIS-2435746, Defense Advanced Research Projects Agency (DARPA) under Contract No. HR00112520042, Hyundai America Technical Center, Inc. (HATCI), as well as the University of Michigan MICDE Catalyst Grant Award and MIDAS PODS Grant Award.

References

Samuel G Armato, Geoffrey McLennan, Luc Bidaut, Michael F McNitt-Gray, and Charles R Meyer. The lung image database consortium (LIDC) and image database resource initiative (IDRI): A completed reference database of lung nodules on CT scans. *Medical Physics*, 38:915–931, 2011. doi: 10.1148/radiol.2323032035.

Gabriel Cardoso, Yazid Janati El Idrissi, Sylvain Le Corff, and Eric Moulines. Monte carlo guided diffusion for bayesian linear inverse problems. *arXiv preprint arXiv:2308.07983*, 2023.

Matthew Chan, Maria Molina, and Chris Metzler. Estimating epistemic and aleatoric uncertainty with a single model. *Advances in Neural Information Processing Systems*, 37:109845–109870, 2024.

Haoxuan Chen, Yinuo Ren, Martin Renqiang Min, Lexing Ying, and Zachary Izzo. Solving inverse problems via diffusion-based priors: An approximation-free ensemble sampling approach. *arXiv preprint arXiv:2506.03979*, 2025.

Hyungjin Chung and Jong Chul Ye. Score-based diffusion models for accelerated mri, 2022a. URL <https://arxiv.org/abs/2110.05243>.

Hyungjin Chung and Jong Chul Ye. Score-based diffusion models for accelerated mri. *Medical Image Analysis*, page 102479, 2022b.

Hyungjin Chung, Jeongsol Kim, Michael T Mccann, Marc L Klasky, and Jong Chul Ye. Diffusion posterior sampling for general noisy inverse problems. *arXiv preprint arXiv:2209.14687*, 2022.

I Craig and J Brown. *Inverse problems in astronomy*. Adam Hilger Ltd., Accord, MA, 12 1985. URL <https://www.osti.gov/biblio/5734250>.

Giannis Daras, Hyungjin Chung, Chieh-Hsin Lai, Yuki Mitsufuji, Jong Chul Ye, Peyman Milanfar, Alexandros G. Dimakis, and Mauricio Delbracio. A survey on diffusion models for inverse problems, 2024. URL <https://arxiv.org/abs/2410.00083>.

Zehao Dou and Yang Song. Diffusion posterior sampling for linear inverse problem solving: A filtering perspective. In *The Twelfth International Conference on Learning Representations*, 2024. URL <https://openreview.net/forum?id=tplXNcHZs1>.

Jonathan Ho, Ajay Jain, and Pieter Abbeel. Denoising diffusion probabilistic models, 2020. URL <https://arxiv.org/abs/2006.11239>.

Paul Hofman, Yusuf Sale, and Eyke Hüllermeier. Quantifying aleatoric and epistemic uncertainty with proper scoring rules. *arXiv preprint arXiv:2404.12215*, 2024.

Eyke Hüllermeier and Willem Waegeman. Aleatoric and epistemic uncertainty in machine learning: an introduction to concepts and methods. *Machine Learning*, 110(3):457–506, March 2021. ISSN 1573-0565. doi: 10.1007/s10994-021-05946-3. URL <http://dx.doi.org/10.1007/s10994-021-05946-3>.

Ajil Jalal, Marius Arvinte, Giannis Daras, Eric Price, Alexandros G. Dimakis, and Jonathan I. Tamir. Robust compressed sensing mri with deep generative priors, 2021. URL <https://arxiv.org/abs/2108.01368>.

Zahra Kadkhodaie and Eero Simoncelli. Stochastic solutions for linear inverse problems using the prior implicit in a denoiser. In M. Ranzato, A. Beygelzimer,

Y. Dauphin, P.S. Liang, and J. Wortman Vaughan, editors, *Advances in Neural Information Processing Systems*, volume 34, pages 13242–13254. Curran Associates, Inc., 2021. URL https://proceedings.neurips.cc/paper_files/paper/2021/file/6e28943943dbed3c7f82fc05f269947a-Paper.pdf.

Tero Karras, Miika Aittala, Samuli Laine, and Timo Aila. Elucidating the design space of diffusion-based generative models. In *Proceedings of the 36th International Conference on Neural Information Processing Systems*, NIPS '22, Red Hook, NY, USA, 2022. Curran Associates Inc. ISBN 9781713871088.

Bahjat Kawar, Michael Elad, Stefano Ermon, and Jiaming Song. Denoising diffusion restoration models. In *Advances in Neural Information Processing Systems*, 2022a.

Bahjat Kawar, Michael Elad, Stefano Ermon, and Jiaming Song. Denoising diffusion restoration models, 2022b. URL <https://arxiv.org/abs/2201.11793>.

Alex Kendall and Yarin Gal. What uncertainties do we need in bayesian deep learning for computer vision? In I. Guyon, U. Von Luxburg, S. Bengio, H. Wallach, R. Fergus, S. Vishwanathan, and R. Garnett, editors, *Advances in Neural Information Processing Systems*, volume 30. Curran Associates, Inc., 2017. URL https://proceedings.neurips.cc/paper_files/paper/2017/file/2650d6089a6d640c5e85b2b88265dc2b-Paper.pdf.

Namhoon Kim and Sara Fridovich-Keil. Towards distribution-shift uncertainty estimation for inverse problems with generative priors, 2025. URL <https://arxiv.org/abs/2510.10947>.

Jean-Marie Lemercier, Julius Richter, Simon Welker, Eloi Moliner, Vesa Välimäki, and Timo Gerkmann. Diffusion models for audio restoration: A review [special issue on model-based and data-driven audio signal processing]. *IEEE Signal Processing Magazine*, 41(6):72–84, 2025.

P. Li, S. Wang, T. Li, J. Lu, Y. HuangFu, and D. Wang. A large-scale ct and pet/ct dataset for lung cancer diagnosis (lung-pet-ct-dx), 2020. URL <https://doi.org/10.7937/TCIA.2020.NNC2-0461>.

Morteza Mardani, Jiaming Song, Jan Kautz, and Arash Vahdat. A variational perspective on solving inverse problems with diffusion models. *arXiv preprint arXiv:2305.04391*, 2023a.

Morteza Mardani, Jiaming Song, Jan Kautz, and Arash Vahdat. A variational perspective on solving inverse problems with diffusion models. *arXiv preprint arXiv:2305.04391*, 2023b.

Eloi Moliner, Jaakko Lehtinen, and Vesa Välimäki. Solving audio inverse problems with a diffusion model. In *ICASSP 2023 - 2023 IEEE International Conference on Acoustics, Speech and Signal Processing (ICASSP)*, pages 1–5, 2023. doi: 10.1109/ICASSP49357. 2023.10095637.

Joseph B Nagel and Bruno Sudret. A unified framework for multilevel uncertainty quantification in bayesian inverse problems. *Probabilistic Engineering Mechanics*, 43: 68–84, 2016.

Leonid I. Rudin, Stanley Osher, and Emad Fatemi. Nonlinear total variation based noise removal algorithms. *Physica D: Nonlinear Phenomena*, 60(1):259–268, 1992. ISSN 0167-2789. doi: [https://doi.org/10.1016/0167-2789\(92\)90242-F](https://doi.org/10.1016/0167-2789(92)90242-F). URL <https://www.sciencedirect.com/science/article/pii/016727899290242F>.

Bowen Song, Soo Min Kwon, Zecheng Zhang, Xinyu Hu, Qing Qu, and Liyue Shen. Solving inverse problems with latent diffusion models via hard data consistency, 2024. URL <https://arxiv.org/abs/2307.08123>.

Jiaming Song, Chenlin Meng, and Stefano Ermon. Denoising diffusion implicit models, 2022a. URL <https://arxiv.org/abs/2010.02502>.

Jiaming Song, Arash Vahdat, Morteza Mardani, and Jan Kautz. Pseudoinverse-guided diffusion models for inverse problems. In *International Conference on Learning Representations*, 2023a.

Jiaming Song, Arash Vahdat, Morteza Mardani, and Jan Kautz. Pseudoinverse-guided diffusion models for inverse problems. In *International Conference on Learning Representations*, 2023b. URL https://openreview.net/forum?id=9_gsMA8MRKQ.

Yang Song, Jascha Sohl-Dickstein, Diederik P. Kingma, Abhishek Kumar, Stefano Ermon, and Ben Poole. Score-based generative modeling through stochastic differential equations, 2021. URL <https://arxiv.org/abs/2011.13456>.

Yang Song, Liyue Shen, Lei Xing, and Stefano Ermon. Solving inverse problems in medical imaging with score-based generative models, 2022b. URL <https://arxiv.org/abs/2111.08005>.

J. Virieux and S. Operto. An overview of full-waveform inversion in exploration geophysics. *Geophysics*, 74(6):WCC1–WCC26, 12 2009. ISSN 0016-8033. doi: 10.1190/1.3238367. URL <https://doi.org/10.1190/1.3238367>.

Yinhuai Wang, Jiwen Yu, and Jian Zhang. Zero-shot image restoration using denoising diffusion null-space model. *The Eleventh International Conference on Learning Representations*, 2023.

David Wiesner, David Svoboda, Martin Maška, and Michal Kozubek. Cytopacq: a web-interface for simulating multi-dimensional cell imaging. *Bioinformatics*, 35(21):4531–4533, 2019.

Zihui Wu, Yu Sun, Yifan Chen, Bingliang Zhang, Yisong Yue, and Katherine Bouman. Principled probabilistic imaging using diffusion models as plug-and-play priors. In *The Thirty-eighth Annual Conference on Neural Information Processing Systems*, 2024. URL <https://openreview.net/forum?id=Xq9HQf7VNV>.

Carl Wunsch. *The Ocean Circulation Inverse Problem*. Cambridge University Press, 1996.

Jure Zbontar, Florian Knoll, Anuroop Sriram, Tullie Murrell, Zhengnan Huang, Matthew J. Muckley, Aaron Defazio, Ruben Stern, Patricia Johnson, Mary Bruno, Marc Parente, Krzysztof J. Geras, Joe Katsnelson, Hersh Chandarana, Zizhao Zhang, Michal Dzodziyal, Adriana Romero, Michael Rabbat, Pascal Vincent, Nafissa Yakubova, James Pinkerton, Duo Wang, Erich Owens, C. Lawrence Zitnick, Michael P. Recht, Daniel K. Sodickson, and Yvonne W. Lui. fastmri: An open dataset and benchmarks for accelerated mri, 2019. URL <https://arxiv.org/abs/1811.08839>.

Bingliang Zhang, Wenda Chu, Julius Berner, Chenlin Meng, Anima Anandkumar, and Yang Song. Improving diffusion inverse problem solving with decoupled noise annealing, 2024. URL <https://arxiv.org/abs/2407.01521>.

Hongkai Zheng, Wenda Chu, Bingliang Zhang, Zihui Wu, Austin Wang, Berthy Feng, Caifeng Zou, Yu Sun, Nikola Borislavov Kovachki, Zachary E Ross, Katherine Bouman, and Yisong Yue. Inversebench: Benchmarking plug-and-play diffusion priors for inverse problems in physical sciences. In *The Thirteenth International Conference on Learning Representations*, 2025. URL <https://openreview.net/forum?id=U3PBIXNG6>.

Yuanzhi Zhu, Kai Zhang, Jingyun Liang, Jiezheng Cao, Bihan Wen, Radu Timofte, and Luc Van Gool. Denoising diffusion models for plug-and-play image restoration. In *IEEE Conference on Computer Vision and Pattern Recognition Workshops (NTIRE)*, 2023.

A Additional Real Data Experiment Results

A.1 Tables of the main results

Table 3: Linear inverse scattering reconstruction performance under different numbers of receivers. PSNR/SSIM are reported as mean \pm standard deviation. Avg Pixel Var is scaled by $\times 10^4$.

Method	Receiver = 360					Receiver = 180				
	PSNR (mean \pm std)	Max PSNR	SSIM (mean \pm std)	Max SSIM	Pixel Var	PSNR (mean \pm std)	Max PSNR	SSIM (mean \pm std)	Max SSIM	Pixel Var
REDDiff	36.216 \pm 0.122	36.476	0.981 \pm 0.000	0.983	0.320	35.053 \pm 0.113	35.352	0.984 \pm 0.000	0.985	0.720
DPS	31.598 \pm 0.188	32.093	0.876 \pm 0.111	0.981	4.020	31.375 \pm 0.181	31.720	0.856 \pm 0.109	0.980	4.060
DAPS	28.740 \pm 0.105	29.014	0.650 \pm 0.003	0.657	9.980	27.064 \pm 0.087	27.267	0.580 \pm 0.003	0.585	15.690
DiffPIR	32.400 \pm 0.164	32.915	0.951 \pm 0.002	0.956	1.700	32.158 \pm 0.149	32.572	0.944 \pm 0.001	0.948	1.500
DDNM	36.356 \pm 0.134	36.672	0.937 \pm 0.001	0.940	0.790	35.114 \pm 0.115	35.409	0.920 \pm 0.001	0.923	0.830
DDRM	31.073 \pm 0.050	31.201	0.913 \pm 0.001	0.917	0.790	26.867 \pm 0.012	26.902	0.876 \pm 0.001	0.878	0.300
PnPDM	34.784 \pm 0.173	35.281	0.970 \pm 0.001	0.973	1.740	32.888 \pm 0.262	33.376	0.966 \pm 0.002	0.970	2.420
FPS	30.134 \pm 0.104	30.365	0.745 \pm 0.004	0.753	2.880	27.528 \pm 0.020	27.581	0.670 \pm 0.001	0.673	0.570
MCG-diff	29.270 \pm 0.121	29.565	0.733 \pm 0.004	0.742	3.060	27.350 \pm 0.030	27.407	0.662 \pm 0.001	0.666	0.540

Table 4: MRI reconstruction results under two different acceleration rates. Metrics are computed over $K = 100$ samples per method. PSNR/SSIM are reported as mean \pm standard deviation. Pixel Var is scaled by $\times 10^3$.

Method	AR = 4					AR = 8				
	PSNR (mean \pm std)	Max PSNR	SSIM (mean \pm std)	Max SSIM	Pixel Var	PSNR (mean \pm std)	Max PSNR	SSIM (mean \pm std)	Max SSIM	Pixel Var
REDDiff	31.298 \pm 0.037	31.378	0.743 \pm 0.001	0.747	1.250	29.574 \pm 0.101	29.851	0.693 \pm 0.001	0.695	1.580
DPS	28.069 \pm 0.140	28.371	0.622 \pm 0.004	0.631	3.582	26.659 \pm 0.272	27.180	0.579 \pm 0.012	0.591	5.210
DAPS	25.809 \pm 0.023	25.858	0.427 \pm 0.001	0.430	4.651	25.334 \pm 0.050	25.459	0.401 \pm 0.001	0.403	6.760
DiffPIR	30.209 \pm 0.045	30.336	0.690 \pm 0.002	0.697	1.599	28.873 \pm 0.149	29.164	0.659 \pm 0.001	0.667	2.190
PnPDM	31.781 \pm 0.037	31.854	0.766 \pm 0.001	0.769	0.977	29.148 \pm 0.213	29.676	0.694 \pm 0.001	0.700	1.510

Table 5: 20 view CT reconstruction results under two different datasets. Metrics are computed over $K = 100$ samples per method. PSNR/SSIM are reported as mean \pm standard deviation. Pixel Var is scaled by $\times 10^3$.

Method	in-distribution					out-of-distribution				
	PSNR (mean \pm std)	Max PSNR	SSIM (mean \pm std)	Max SSIM	Pixel Var	PSNR (mean \pm std)	Max PSNR	SSIM (mean \pm std)	Max SSIM	Pixel Var
REDDiff	30.755 \pm 0.094	30.987	0.848 \pm 0.002	0.8531	0.298	25.306 \pm 0.094	25.512	0.739 \pm 0.003	0.7471	0.521
DPS	31.333 \pm 0.167	31.804	0.813 \pm 0.023	0.8422	0.305	24.575 \pm 0.190	25.024	0.671 \pm 0.017	0.7040	0.578
DAPS	28.034 \pm 0.082	28.254	0.770 \pm 0.003	0.7779	0.171	24.865 \pm 0.069	25.018	0.701 \pm 0.003	0.7077	0.185
DiffPIR	22.803 \pm 0.214	23.222	0.659 \pm 0.011	0.6789	0.844	19.712 \pm 0.100	19.981	0.506 \pm 0.010	0.5294	0.901
PnPDM	27.619 \pm 0.568	28.827	0.803 \pm 0.010	0.8259	0.329	24.049 \pm 0.229	24.450	0.701 \pm 0.006	0.7128	0.464

Table 6: MRI reconstruction results under AR=4 across with additional five test cases. Metrics are computed over $K = 100$ samples per method. PSNR/SSIM are reported as mean \pm standard deviation. Pixel Var is scaled by $\times 10^3$.

Method	PSNR (mean \pm std)	Max PSNR	SSIM (mean \pm std)	Max SSIM	Pixel Var	PSNR (mean \pm std)	Max PSNR	SSIM (mean \pm std)	Max SSIM	Pixel Var
Test Image 1										
REDDiff	26.651 \pm 0.009	26.669	0.497 \pm 0.000	0.499	0.253	29.111 \pm 0.018	29.150	0.670 \pm 0.000	0.672	0.263
DPS	24.272 \pm 0.094	24.471	0.379 \pm 0.005	0.388	4.749	25.443 \pm 0.105	25.672	0.467 \pm 0.005	0.480	5.288
DAPS	19.017 \pm 0.020	19.059	0.189 \pm 0.001	0.195	9.334	20.897 \pm 0.019	20.947	0.264 \pm 0.001	0.267	7.918
DiffPIR	26.134 \pm 0.039	26.220	0.474 \pm 0.002	0.479	1.868	27.415 \pm 0.046	27.527	0.577 \pm 0.002	0.583	2.314
PnPDM	26.200 \pm 0.848	26.448	0.536 \pm 0.003	0.541	2.141	28.523 \pm 0.036	28.625	0.671 \pm 0.001	0.674	1.583
Test Image 3										
REDDiff	29.476 \pm 0.024	29.538	0.500 \pm 0.002	0.506	0.058	31.634 \pm 0.020	31.678	0.751 \pm 0.000	0.752	0.078
DPS	26.706 \pm 0.164	27.119	0.649 \pm 0.005	0.660	1.641	27.520 \pm 1.453	28.137	0.685 \pm 0.006	0.693	2.975
DAPS	23.762 \pm 0.047	23.869	0.351 \pm 0.002	0.356	2.408	26.982 \pm 0.031	27.068	0.522 \pm 0.002	0.527	2.111
DiffPIR	28.008 \pm 0.093	28.187	0.700 \pm 0.002	0.705	0.820	29.119 \pm 0.060	29.253	0.736 \pm 0.002	0.742	1.110
PnPDM	26.741 \pm 4.129	29.306	0.690 \pm 0.030	0.715	4.985	31.066 \pm 0.029	31.145	0.805 \pm 0.001	0.808	0.471
Test Image 5										
Average across 5 test cases										
REDDiff	24.005 \pm 4.049	30.985	0.507 \pm 0.028	0.565	3.345	28.175		0.585		0.799
DPS	27.397 \pm 0.695	27.765	0.687 \pm 0.007	0.703	1.262	26.268		0.573		3.183
DAPS	24.657 \pm 0.055	24.757	0.355 \pm 0.002	0.359	1.838	23.063		0.336		4.722
DiffPIR	28.544 \pm 0.084	28.752	0.796 \pm 0.001	0.799	0.659	27.844		0.657		1.354
PnPDM	29.038 \pm 3.687	30.601	0.824 \pm 0.035	0.839	2.813	28.314		0.705		2.399

A.2 Additional reconstruction and variance figures

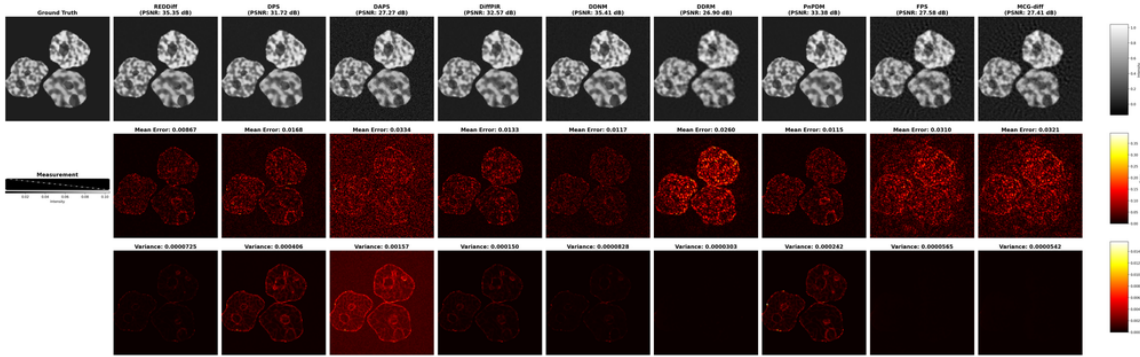


Figure 11: Linear inverse scattering with 180 receivers.

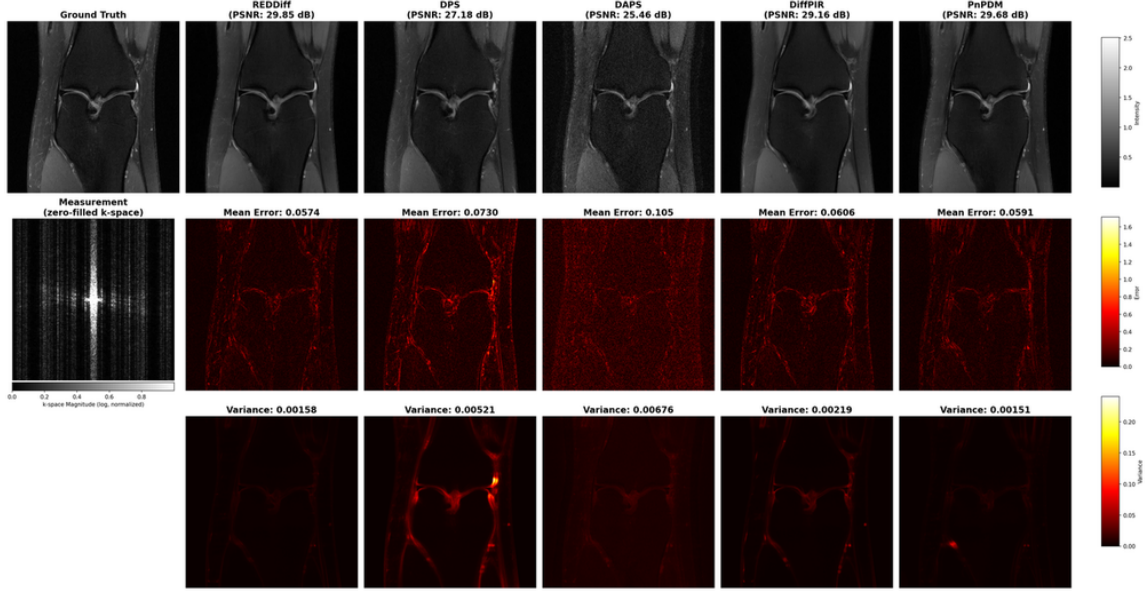


Figure 12: Compressed sensing MRI with AR=8.

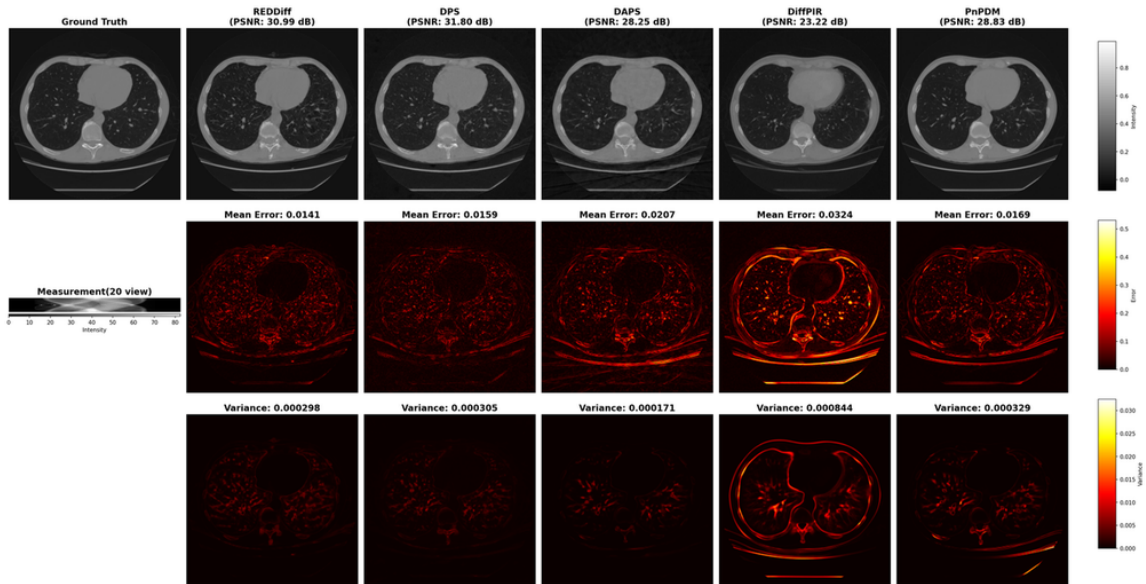


Figure 13: Sparse view CT with in distribution test image

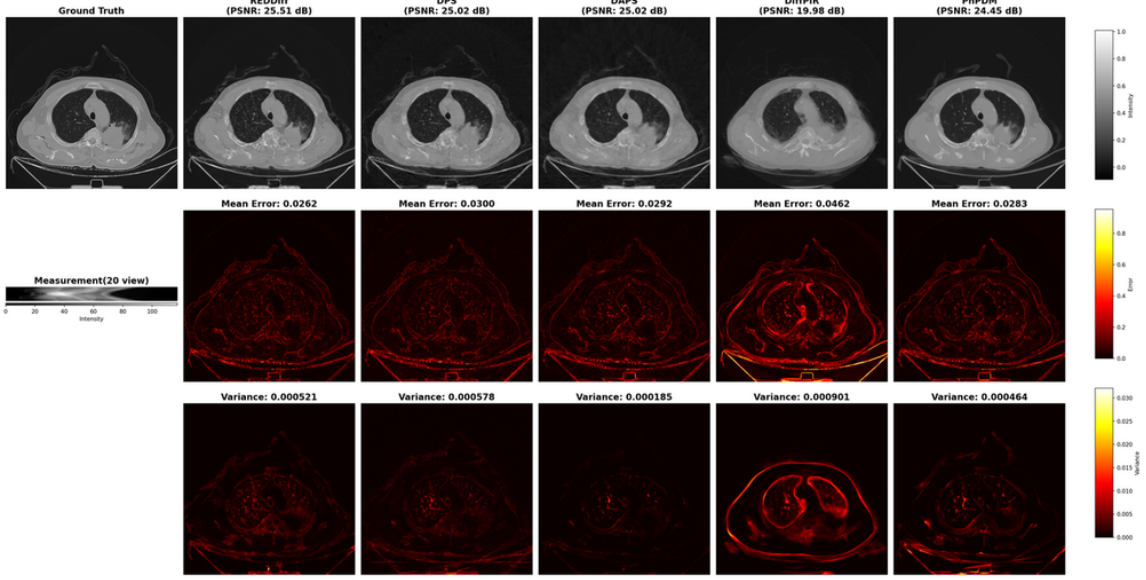


Figure 14: Sparse view CT with out of distribution test image

A.3 Hyperparameters analysis of *Posterior targetin solvers*

For the particle-based posterior targeting solvers, such as FPS and MCG-Diff, theory B.6 and B.4 suggest that as the number of particles N increases, their induced empirical distribution should better approximate the target posterior, improving the reliability of uncertainty estimates. Consistent with this expectation, in the sparse linear inverse scattering setting with 180 receivers, we observe that small particle sizes lead to degraded and unstable variance estimates, indicative of particle degeneracy and poor posterior approximation. Increasing the particle size to $N = 64$ substantially stabilizes the empirical variance and produces more coherent uncertainty maps, while the reconstruction accuracy (e.g., PSNR) remains almost unchanged. This highlights that, in practice, particle count can primarily affect uncertainty quality rather than point accuracy in terms of the distribution estimation.

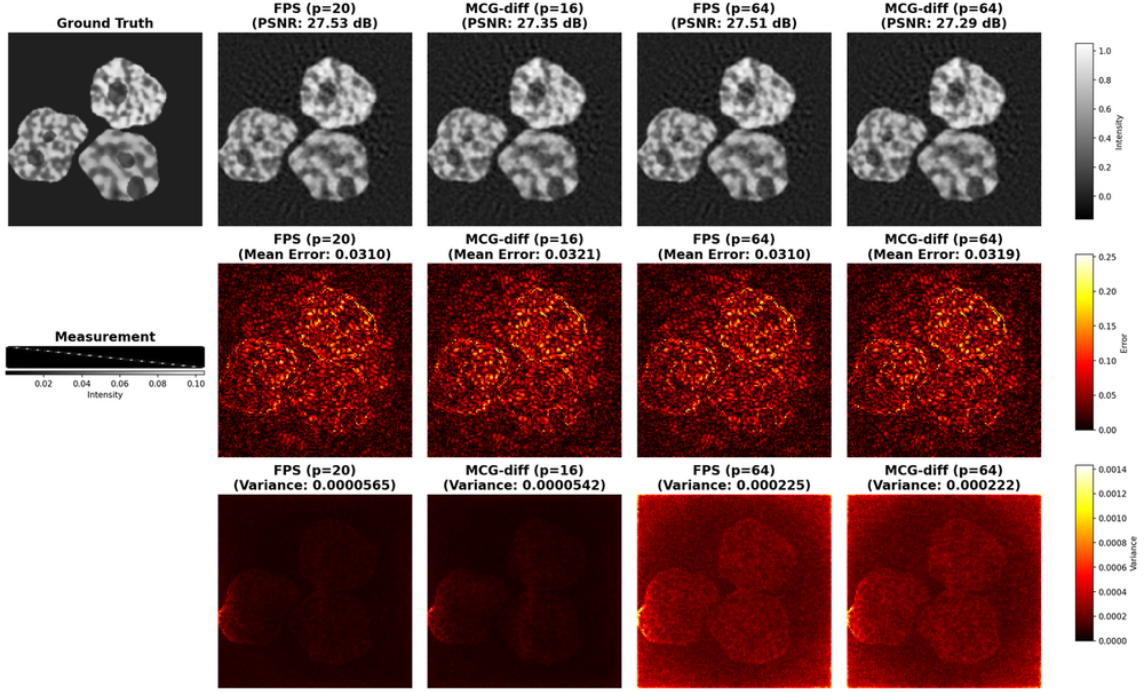


Figure 15: FPS and MCG-Diff under linear inverse scattering with 180 receivers: effect of particle count on uncertainty. Left two: runs with small particle sizes (FPS: $N = 20$; MCG-Diff: $N = 16$) show degraded uncertainty estimates. Right two: increasing the particle size to $N = 64$ for both solvers yields more moderate empirical variance, while the reconstruction accuracy remains nearly unchanged.

Table 7: MRI reconstruction results on $AR = 4$ for FPS and MCG-Diff with different particle size (p). Pixel Var is scaled by $\times 10^4$

Method	PSNR (avg \pm std)	PSNR (max)	SSIM (avg \pm std)	SSIM (max)	Avg(Pixel Var)
FPS (p=20)	27.528 ± 0.020	27.581	0.670 ± 0.001	0.673	0.57
MCG-diff (p=16)	27.350 ± 0.030	27.407	0.662 ± 0.001	0.666	0.54
FPS (p=64)	27.515 ± 0.025	27.609	0.668 ± 0.003	0.677	2.25
MCG-diff (p=64)	27.294 ± 0.033	27.375	0.662 ± 0.003	0.668	2.22

We also observe a uncertainty-PSNR trade-off regarding the hyperparameter learning rate η in PnPDM shown in figure 16. Increasing the Langevin step size η from 10^{-6} to 10^{-4} in MRI with $AR=4$, increased the empirical pixel-wise variance while reduced the reconstruction PSNR by about 1.5dB.

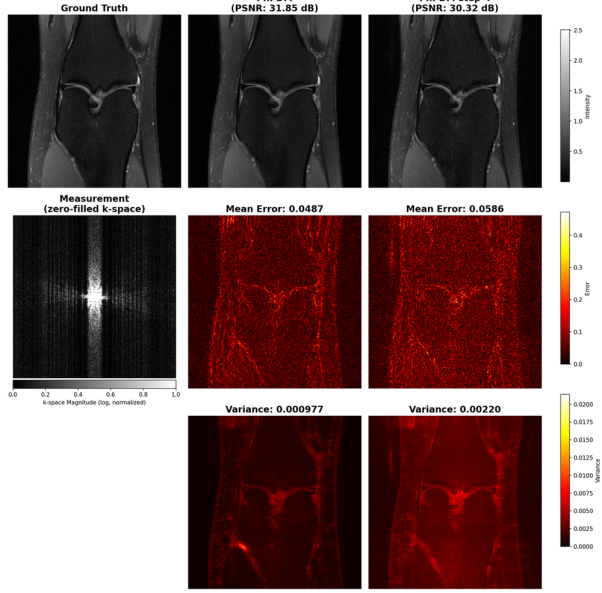


Figure 16: PnPDM MRI AR=4, the left is with learning rate $\eta = 10^{-6}$, the right is with learning rate $\eta = 10^{-4}$, the remaining hyperparameters keep the same as [Zheng et al., 2025].

B Theoretical guarantee for posterior targeting samplers

B.1 Notations and Preliminaries

Let $x \in \mathbb{R}^n$ and $y \in \mathbb{R}^m$ denote the unknown signal and the observed measurement, respectively. We denote the forward operator as $A : \mathbb{R}^n \rightarrow \mathbb{R}^m$ and the data fidelity potential as $f(x; y) := -\log p(y|x)$. In the diffusion context, $\{x_t\}_{t=0}^T$ denotes the trajectory with noise schedule $\sigma(t)$, and $s_\theta(x, t)$ represents the learned score network.

B.2 PnP-DM: convergence to a stationary split posterior and approximation to $p(x | y)$

PnP-DM admits a principled interpretation via the Split Gibbs Sampler (SGS) [Wu et al., 2024]. The target Bayesian posterior is

$$p(x | y) \propto \exp(-f(x; y) - g(x)), \quad (3)$$

where $f(x; y) := -\log p(y | x)$ and $g(x) := -\log p(x)$. SGS instead targets the split joint distribution

$$\pi_\rho(x, z) \propto \exp\left(-f(z; y) - g(x) - \frac{1}{2\rho^2} \|x - z\|_2^2\right), \quad (4)$$

with x -marginal $\pi_{\rho,X}$. As $\rho \rightarrow 0$, $\pi_{\rho,X} \rightarrow p(x \mid y)$.

Assumption B.1. To connect the PnP-DM iterate distribution to the true posterior, we separate three sources of error:

1. **(Score accuracy)** In the ideal case, the diffusion score is exact, i.e., $s_\theta(x_t, t) = \nabla_{x_t} \log p_t(x_t)$ (equivalently $\varepsilon_{\text{score}} = 0$).
2. **(Convergence from initialization)** The Markov chain is run sufficiently long so that the initialization-dependent term vanishes, i.e., $K \rightarrow \infty$ (hence $T = K(t^* + 1) \rightarrow \infty$) with a fixed $\rho > 0$ and regular schedule constants bounded away from 0.
3. **(Split bias)** The coupling parameter $\rho \rightarrow 0$, so that the split marginal $\pi_{\rho,X}$ approaches the exact posterior $p(x \mid y)$.

Theorem B.2 (PnP-DM convergence bound (Theorem 3.1 in [Wu et al., 2024])). *Consider running K iterations of PnP-DM with a constant coupling $\rho_k \equiv \rho > 0$ and a score estimate s_t . Let $t^* > 0$ satisfy $\sigma(t^*) = \rho$, and define*

$$v(t) := s(t) \sqrt{2\dot{\sigma}(t) \sigma(t)}, \quad \delta := \inf_{t \in [0, t^*]} v(t),$$

as in [Wu et al., 2024]. Let ν_τ and π_τ denote the distributions at time τ of the non-stationary and stationary processes, respectively. Over $\tau \in [0, T]$ with $T := K(t^* + 1)$, we have:

$$\frac{1}{T} \int_0^T \text{FI}(\pi_\tau \parallel \nu_\tau) d\tau \leq \underbrace{\frac{4 \text{KL}(\pi_X \parallel \nu_{0,X})}{K(t^* + 1) \min(\rho, \delta)^2}}_{\text{convergence from initialization}} + \underbrace{\frac{4 \varepsilon_{\text{score}}}{(t^* + 1) \delta^2}}_{\text{score approximation error}}, \quad (5)$$

where π_X and $\nu_{0,X}$ are the x -marginals of π_τ and ν_0 , and

$$\varepsilon_{\text{score}} := \int_{t^*+1} \frac{1}{v(\tau)^2} \mathbb{E}_{\pi_\tau} \left\| s_\tau - \nabla \log p_\tau \right\|_2^2 d\tau < \infty.$$

Proof The proof of Theorem B.2 is given in Appendix A.2 of [Wu et al., 2024].

Interpretation on the convergence. The bound in (5) separates two effects: (i) a *finite-iteration* term that decays as $O(1/K)$ for fixed ρ and $\delta > 0$, and (ii) a *score approximation* term that acts as an error floor. Under Assumption (1) and (2) in B.1 (perfect score, run the chain long enough with fixed $\rho > 0$ and regular schedule so that $\delta > 0$), the right-hand side of (5) vanishes as $K \rightarrow \infty$:

$$\varepsilon_{\text{score}} = 0, \rho > 0, \delta > 0 \implies \lim_{K \rightarrow \infty} \frac{1}{T} \int_0^T \text{FI}(\pi_\tau \parallel \nu_\tau) d\tau = 0. \quad (6)$$

That is, the non-stationary PnP-DM process approaches the corresponding x -marginal $\pi_{\rho,X}$ in the averaged Fisher-information sense.

Assumption (3) in B.1 controls the remaining *split bias*: as $\rho \rightarrow 0$, the stationary x -marginal $\pi_{\rho,X}$ converges to the target posterior $p(x \mid y)$ in total variation distance. Combining these two limits yields an “approximate posterior sampling” guarantee: for sufficiently large K (to reduce the initialization term) and sufficiently small ρ (to reduce the split bias), samples produced by PnP-DM are close to draws from $p(x \mid y)$, up to the score-error floor when $\varepsilon_{\text{score}} > 0$.

Trade-off between K and ρ . Note that the initialization term in (5) scales with $\min(\rho, \delta)^{-2}$; therefore taking ρ extremely small can slow down the $O(1/K)$ decay, requiring larger K to reach the stationary regime. In practice, one selects ρ to balance this mixing-versus-bias trade-off.

B.3 MCG-Diff [Cardoso et al., 2023]

Assumption B.3 (Ideal diffusion prior for MCG-Diff (perfect score and vanishing discretization)). Assume:

1. **(Score accuracy).** The learned score is exact, i.e., $s_\theta(x_t, t) = \nabla_{x_t} \log p_t(x_t)$ for all t .
2. **(Accurate reverse solver).** The reverse-time ODE/SDE solver is asymptotically exact as the step size $\Delta t \rightarrow 0$ (equivalently, the discretization grid is refined so that the induced reverse transition kernel matches the continuous-time reverse dynamics).

Remark. Let $\lambda_{t-1}(x_{t-1} \mid x_t)$ denote the learned backward kernel used to sample the reverse trajectory. Under Assumption B.3(1)–(2), the induced discrete reverse transition kernel $\lambda_{t-1}(x_{t-1} \mid x_t)$ coincides with the time-reversal of the forward diffusion kernel $q_t(x_t \mid x_{t-1})$, which is the “model consistency” condition

$$p_t(x_t) \lambda_{t-1}(x_{t-1} \mid x_t) = p_{t-1}(x_{t-1}) q_t(x_t \mid x_{t-1}), \quad \forall t = 1, \dots, T, \quad (7)$$

used in [Cardoso et al., 2023] Proposition 2.3.

Theorem B.4 (MCG-Diff target and particle approximation (Prop. 2.3 in [Cardoso et al., 2023])). *Let $\{\phi_t^y\}_{t=0}^n$ denote the sequence of guided diffusion-time marginals in [Cardoso et al., 2023], and in particular let $\phi_0^y(x_0)$ denote the target distribution at diffusion time $t = 0$. Assume the reverse kernel $p_t(x_t) \lambda_{t-1}(x_{t-1} \mid x_t) = p_{t-1}(x_{t-1}) q_t(x_t \mid x_{t-1}), \forall t = 1, \dots, T$*

$1, \dots, T$, (as in Assumption B.3). Then ϕ_0^y admits the bridge representation

$$\phi_0^y(x_0) \propto \int \lambda_{0|\tau_1}(x_0 \mid x_{\tau_1}) \phi_{\tau_1:n}^y(dx_{\tau_1:n}), \quad (8)$$

where $\phi_{\tau_1:n}^y$ is the guided path distribution on the segment $\{x_{\tau_1}, \dots, x_n\}$ and $\lambda_{0|\tau_1}$ denotes the composed reverse transition from time τ_1 to 0.

Interpretation and posterior implication. The right-hand side of (8) provides a two-stage sampling recipe for the time-0 target ϕ_0^y : (i) sample a guided diffusion-time path segment $(x_{\tau_1}, \dots, x_n) \sim \phi_{\tau_1:n}^y$ (in MCG-Diff this is approximated by a particle filter using SMC), and (ii) propagate the state x_{τ_1} back to time 0 by sampling $x_0 \sim \lambda_{0|\tau_1}(\cdot \mid x_{\tau_1})$ via repeated reverse-diffusion transitions. Thus, (8) is a *generative representation* of the time = 0 marginal: it guarantees that the resulting x_0 has marginal density ϕ_0^y (up to normalization). Moreover, in MCG-Diff the guided potentials defining $\{\phi_t^y\}$ are constructed from the measurement likelihood, so that $\phi_0^y(x_0) \propto p(y \mid x_0)p_0(x_0)$ and hence $\phi_0^y(\cdot) = p(\cdot \mid y)$ after normalization. To sum up, MCG-Diff approximates $\phi_{\tau_1:n}^y$ with a particle filter based on SMC, which returns a set of particles with importance weights whose empirical distribution converges to $\phi_{\tau_1:n}^y$ as $N \rightarrow \infty$. Propagating these particles back to time 0 via $\lambda_{0|\tau_1}$ therefore yields an empirical distribution at time 0 that converges to ϕ_0^y , i.e., to the Bayesian posterior $p(x_0 \mid y)$ after normalization.

Proof. This is given in Proposition 2.3 and Appendix B.2 in [Cardoso et al., 2023].

B.4 FPS-SMC[Dou and Song, 2024]

Assumption B.5. Assume the following two fact:

1. **Score accuracy.** The score model is exact for the diffusion marginal, i.e., $s_\theta(x_t, t) = \nabla_{x_t} \log p_t(x_t)$ for all t .
2. **Vanishing discretization error.** The reverse-time ODE/SDE solver is asymptotically exact as the step size $\Delta t = T/N \rightarrow 0$, so that the backward diffusion dynamics incur no discretization error.

Theorem B.6 (Asymptotic consistency of FPS-SMC [Dou and Song, 2024]). *Let $p_\theta(x_{0:N} \mid y_{0:N})$ denote the joint distribution over the diffusion-time path produced by FPS-SMC with M particles, and let $p^*(x_{0:N} \mid y_{0:N})$ denote the solution to the corresponding Bayesian filtering problem defined on the (ideal) diffusion model. Under Assumption B.5, the conditional reverse kernels match, $p_\theta(x_k \mid x_{k+1}) = p^*(x_k \mid x_{k+1})$ for all $k = 0, 1, \dots, N-1$.*

Moreover, as $M \rightarrow \infty$ (and $N \rightarrow \infty$ so that $\Delta t \rightarrow 0$), the marginal at $t = 0$ is asymptotically consistent:

$$p_\theta(x_0 | y_0) \Rightarrow p^*(x_0 | y_0) = q(x_0 | y_0), \quad M \rightarrow \infty, \quad (9)$$

where \Rightarrow denotes weak convergence and $q(x_0 | y_0)$ is the target posterior induced by the diffusion prior and likelihood.

Proof and interpretation. The proof is given in Appendix D.2 in [Dou and Song, 2024]. It shows that, under ideal score and vanishing time discretization, FPS-SMC implements the correct reverse-time filtering dynamics, and then applying the standard particle approximation argument to obtain weak convergence as the particle size $M \rightarrow \infty$.

C The convergence of variance estimates versus the number of runs

To ensure our uncertainty quantification is using the stable empirical variance, we studied that how many reconstructions are required to achieve the convergence of the variance estimation. As shown in Figure 17, we repeatedly run DPS on MRI with AR=4, and calculate the variance using the first k reconstructions for 20 random pixels. We observed that most pixels stabilize after 40 runs, and all pixels come to stable around 80-100 runs. We therefore set $K = 100$ to ensure the stable empirical variance estimation.

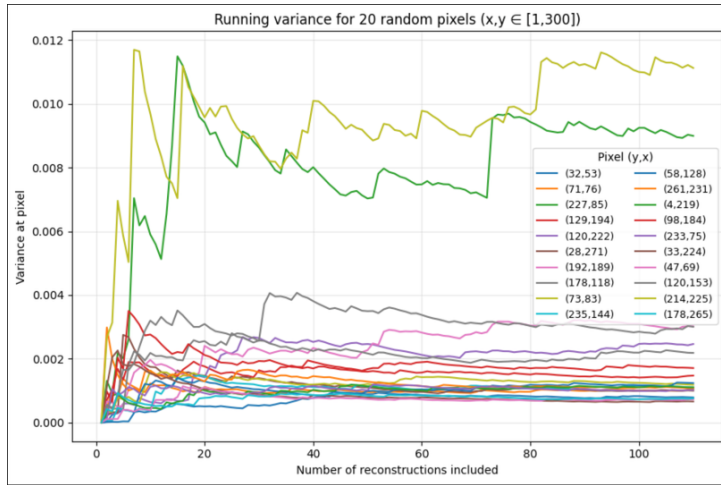


Figure 17: For a fixed MRI test measurement, we run DPS repeatedly with independent randomness and compute the empirical variance of 20 pixels using first K reconstructions. We plot the relationship of pixel variance and the number of reconstruction included. The curve stabilizes after $K \approx 80 - 100$, motivating our default choice $K = 100$ in all experiments.

D Toy simulations

D.1 Experiment setups

Prior. Let $z \in \mathbb{R}^{16}$ and split $z = (z_s, z_w)$ with $z_s \in \mathbb{R}^8$ (dims 0–7) and $z_w \in \mathbb{R}^8$ (dims 8–15). We use an equally-weighted two-component Gaussian mixture

$$p(z) = \frac{1}{2} \mathcal{N}(z; \mu^{(-)}, \Sigma) + \frac{1}{2} \mathcal{N}(z; \mu^{(+)}, \Sigma),$$

with block-diagonal covariance $\Sigma = \text{diag}(\Sigma_s, \Sigma_w)$, where $(\Sigma_s)_{ij} = \rho^{|i-j|}$ for $i, j \in \{0, \dots, 7\}$ with $\rho = 0.8$ and $\Sigma_w = \sigma_w^2 I_8$ with $\sigma_w^2 = 5.0$. The means differ only in coordinate 7 of the structured block:

$$\mu^{(\pm)} = \begin{bmatrix} \mu_s^{(\pm)} \\ 0 \end{bmatrix}, \quad \mu_s^{(\pm)} = (0, \dots, 0, \pm\mu)^\top, \quad \mu = 2.0,$$

so $z_s[0:6]$ are zero-mean but correlated, $z_s[7]$ is bimodal, and z_w are independent high-variance Gaussians.

Diffusion prior training. We train a noise-prediction MLP on $N = 50,000$ samples from the toy prior, stored as tensors of shape $[N, 1, 4, 4]$ (16D reshaped to $1 \times 4 \times 4$). We optimize the standard denoising objective

$$\mathcal{L}(\theta) = \mathbb{E} \left[\|\hat{\epsilon}_\theta(x_\sigma, \sigma) - \epsilon\|_2^2 \right], \quad x_\sigma = x_0 + \sigma\epsilon, \quad \epsilon \sim \mathcal{N}(0, I),$$

D.2 Experiment procedures

Algorithm 1 Experiment 1: Measurement Uncertainty Recovery Evaluation

Input: Measurements $\{y^{(n)}\}_{n=1}^N$, Ground truth $\{x^{*(n)}\}_{n=1}^N$, Solver \mathcal{S}

Parameter: Confidence level $\alpha = 0.95$ (critical value $z_{\alpha/2} = 1.96$)

for $n = 1$ to N do

 Draw K samples: $\{x^{(k,n)}\}_{k=1}^K \sim \mathcal{S}(y^{(n)})$
 for $j = 1$ to d do
 $\hat{\mu}_j^{(n)} \leftarrow \frac{1}{K} \sum_{k=1}^K x_j^{(k,n)}$
 $\hat{\sigma}_j^{2(n)} \leftarrow \frac{1}{K-1} \sum_{k=1}^K (x_j^{(k,n)} - \hat{\mu}_j^{(n)})^2$
 $\text{CI}_j^{(n)} \leftarrow [\hat{\mu}_j^{(n)} - 1.96\hat{\sigma}_j^{(n)}, \hat{\mu}_j^{(n)} + 1.96\hat{\sigma}_j^{(n)}]$
 $c_j^{(n)} \leftarrow \mathbf{1}\{x_j^{*(n)} \in \text{CI}_j^{(n)}\}$
 end for

end for

Output: Coverage_{global} = $\frac{1}{Nd} \sum_{n=1}^N \sum_{j=1}^d c_j^{(n)}$

Algorithm 2 Experiment 2: Observed vs. Null-Space Variance Evaluation

Input: Test observations $\{y^{(n)}\}_{n=1}^N$, SVD basis V of A (right singular vectors), singular values $\{S_j\}_{j=1}^d$, solver \mathcal{S}

Parameters: Number of test cases $N = 20$, number of runs $K = 100$

Output: Per-dimension variance $\{\bar{\sigma}_j^2\}_{j=1}^d$, summary statistics $\text{Var}_{\text{obs}}, \text{Var}_{\text{null}}$

Initialize $\bar{\sigma}_j^2 \leftarrow 0$ for all $j = 1, \dots, d$

for $n = 1$ **to** N **do**

- Draw K samples: $\{x^{(k,n)}\}_{k=1}^K \sim \mathcal{S}(y^{(n)})$
- for** $k = 1$ **to** K **do**

 - Project to SVD coordinates: $z^{(k,n)} \leftarrow V^\top x^{(k,n)}$
 - end for**
 - for** $j = 1$ **to** d **do**

 - Compute sample variance in dimension j : $\hat{\sigma}_j^{2(n)} \leftarrow \text{Var}(\{z_j^{(k,n)}\}_{k=1}^K)$
 - Accumulate: $\bar{\sigma}_j^2 \leftarrow \bar{\sigma}_j^2 + \hat{\sigma}_j^{2(n)}$
 - end for**

 - end for**

Average over test cases: $\bar{\sigma}_j^2 \leftarrow \frac{1}{N} \bar{\sigma}_j^2$ for all $j = 1, \dots, d$

$\text{Var}_{\text{obs}} \leftarrow \frac{1}{|\{j:S_j=1\}|} \sum_{j:S_j=1} \bar{\sigma}_j^2$

$\text{Var}_{\text{null}} \leftarrow \frac{1}{|\{j:S_j=0\}|} \sum_{j:S_j=0} \bar{\sigma}_j^2$
